Tribol Lett (2013) 50:387–395
DOI 10.1007/s11249-013-0136-8

ORIGINAL PAPER

Tribological Properties Mapping: Local Variation in Friction Coefficient and Adhesion

Rubén Álvarez-Asencio · Jinshan Pan · Esben Thormann · Mark W. Rutland

Received: 31 January 2013 / Accepted: 30 March 2013 / Published online: 11 April 2013

Abstract Tribological properties mapping is a new technique that extracts friction *coefficient* and *adhesion* maps obtained from lateral atomic force microscope (LAFM) images. By imaging the surface systematically as a function of load, a series of images can be tiled, and pixelwise fitted to a modified Amontons' Law to obtain friction coefficient and adhesion maps. This removes the ambiguity of friction contrast in LAFM imaging which can be a function of the load used for imaging. In ambient laboratory, air and tetradecane, a sample of Vancron®40, commercial powder metallurgical tool alloy containing nitrogen, have been scanned using a standard silicon cantilever in order to obtain tribological data. The tribological properties mapping provides unique information regarding the heterogeneous alloy microstructure as well as shedding light on the tribological behavior of the alloy.

Keywords Friction · AFM · Atomic force microscope · LFM · Lateral atomic force microscope · Nanotribology · Friction coefficient mapping · Adhesion · Tool alloy · Microstructure

R. Álvarez-Asencio · J. Pan · E. Thormann · M. W. Rutland
Department of Surface and Corrosion Science, School of Chemical Science and Engineering, KTH Royal Institute of Technology, 100 44 Stockholm, Sweden
e-mail: alvarezr@kth.se

M. W. Rutland (✉)
Chemicals, Materials and Surfaces, SP Technical Research Institute of Sweden, Borås, Sweden
e-mail: mark@kth.se

1 Introduction

In materials with complex microstructure, the different components generally have specific roles to play with regard to the macroscopic properties of the material. In a nanocomposite material, for example, rod-like fibrils may be used to impart strength to an otherwise brittle matrix [1], and biopolymers perform a similar function in, for example, shells and gastroliths [2]. In tool alloys, which contain hard phase particles in the alloy matrix, the particles have a strong influence on the strength, hardness, frictional and corrosion properties [3]. Thus, the *surface* properties of components, as well as their distribution in the surface, are of great importance. Scanning probe technologies now abound for the characterization of materials at the nanoscale, and lateral force microscopy (LFM) has long been a part of this armory. As the scanning tip traverses the surface in contact mode, frictional forces cause a twisting of the cantilever which is easily measured and which provides a sensitive means of obtaining chemical contrast on a surface. While the measured force can be obtained quantitatively, the friction at any point on the surface is a function not only of the constant applied load, but also depends on the local adhesion between tip and surface, which of course varies with the surface composition and microstructure. The friction force, and thus the image contrast, therefore varies depending on the tip, the surface and the ambient conditions. The friction *coefficient* is a more useful measure of the tribological properties, but it is not obtained from conventional LFM measurements.

The friction coefficient dates from studies of friction by Leonardo da Vinci and Guillaume Amontons who both postulated that the lateral friction force (F_f) is directly proportional to the applied load (F_L) and independent of the apparent area of contact according to Eq. 1.

$$F_f = \mu F_L \quad (1)$$

The proportionality between the lateral friction force and the applied load is given by μ, known as the friction coefficient. This parameter allows comparison of the frictional properties between systems and contains more information than the absolute value of friction at an arbitrary load. However, when the adhesive forces in the system are comparable with the applied load, for example, in single asperity contact, the adhesion acts as an additional load that also has to be considered and Eq. 1 is no longer valid. As a result, measureable friction extends to negative applied loads. In the adhesive regime, there can be significant deviation from linearity for soft surfaces, but [4, 5] for hard (and rough) surfaces, the friction–load relationship can often be simplified (by ignoring the contact mechanical deviation from linearity) by the following equation proposed by Derjaguin [6]:

$$F_f(F_L) = \mu F_L + F_f(0) \quad (2)$$

[where F_f (0)] is the friction at zero applied load.

In this simplified, but usually reasonable approximation, the friction coefficient can thus be defined independently of adhesion (in the limit of nondeformable materials) and a measure of the adhesion is obtained from the negative apparent applied load at which the friction force becomes zero [F_L ($F_f = 0$)]. Equation 2 is generally valid for both multi-asperity contacts and adhesive contacts whenever deformation is small over the measured range [7, 8]. This empirical relationship has been proven in many experimental systems [4, 9–13], has a broad range of applicability and is the most common means of quantitatively describing the friction between surfaces [7, 8, 14].

Around 1942, Bowden and Tabor [15] demonstrated that the real contact area between two solids is only a small fraction of the apparent contact area because of surface roughness. At the nanometer/micrometer scale, every surface is rough, and when surfaces are slid with respect each to each other, they make contact at some microscopic contacts (asperities). Hence, in order to get a mechanistic understanding of the friction processes that take place at microcontacts, it is instructive to study friction at the micro- and nanoscales, particularly in the case of multicomponent materials, where the asperities may not be representative of the material as a whole and may in fact be determining for the tribological response.

A lot of effort has thus been devoted recently to the study of micro-/nanotribology employing techniques such as the surface force apparatus (SFA) and atomic force microscope (AFM), especially with lateral AFM (LFM). The friction forces originating from the interaction between the tip and the surface lead to twisting of the cantilever, and this tip–surface interaction is often held to mimic the interactions between microcontacts [16].

LFM has been applied to map a wide range of surfaces, such as thiol monolayers [17], graphite [18], hair [19], biological surfaces [20], polyurethanes [21] and conductive polymers [22], providing qualitative friction images (by sliding the probe's tip across the sample). On the other hand, quantitative friction map measurements are possible but more difficult to obtain. They rely on the conversion of photodiode signal to force which demands the arduous calculation of both the torsional spring constant of the cantilever and lateral deflection sensitivity [23]. These qualitative and quantitative measurements provide useful information about the tip and sample interaction and can be successfully related to the interfacial properties of the sample. However, to completely map the tribological properties of the surface, the adhesion and friction coefficients are required for each pixel—that is, Equation 2 needs to be fitted to the data pointwise.

Breakspear et al. [24] reported in 2004 the first example of friction coefficient mapping where an Si_3N_4 cantilever was used to map a binary polymer blend. This mapping technique was able to provide, for the first time, an image with friction coefficient information in every pixel. As mentioned above, and as is clear from Eq. 2, both the adhesion *and* the friction coefficients are required for a complete tribological description of the surface. Thus, it would be useful if a mapping technique were able to deliver *both* these properties simultaneously.

In this study, a new technique, tribological properties mapping (TPM), has been developed based on LFM data to study friction at the micro-/nanoscale. With this technique, a series of images containing torsional deflection information of the cantilever at different applied loads are converted into two new images in which each pixel represents the friction coefficient and adhesion, respectively. Further, the adhesion is obtained without the need of separating the surfaces. The alloy Vancron®40, a commercial powder metallurgical tool alloy containing nitrogen, was selected for this study, because of its heterogeneous microstructure which allows identification of domains of differing properties. This tool alloy contains a homogeneous distribution of fine hard phase particles of carbides (5 %) and carbide-nitrides (19 %) embedded in a metallic solid solution matrix, where the matrix and the hard phase particles have markedly different material properties [25]. The tool alloy exhibits high hardness and low friction, and it is a goal of this study to attempt to relate such behavior to the exposed surface microstructure. In this study, we demonstrate how the tribological properties of this material can be mapped in both air and tetradecane.

2 Experimental

2.1 Samples

The alloy Vancron®40 was generously provided by Uddeholm (Hagfors, Sweden) and was polished (Labopol-5, Struers, Ballerup, Denmark) using different silicon carbide polishing papers (Struers, Ballerup, Denmark). For the final polishing, several polishing cloths (Struers, Ballerup, Denmark) with different diamond pastes with 3, 1 and 1/4 μm particle size (Struers, Ballerup, Denmark) and an alumina suspension with 0.04 μm particle size were used in order to eliminate any scratches over 30 nm. The sample was cleaned with ethanol (99.5 %, Kemetyl, Haninge, Sweden), after every polishing step. Finally, before measurement, it was rinsed with Milli-Q water (Millipore, Molsheim, France) and ethanol and dried with N_2. The measurements were performed both in air and in tetradecane (99 %, Sigma, Haninge, Sweden).

2.2 Atomic Force Microscopy

A NanoScope IIIa Atomic Force Microscope (Bruker®, Santa Barbara, CA) with the J piezoelectric scanner was used in this work. Rectangular silicon cantilevers (NSC14/ALBS and, NSC36/Cr-Au MikroMasch Estonia) with normal spring constants of 3.5 and 0.8 N/m, respectively, and a nominal tip radius of 10 nm were chosen. These cantilevers were chosen based on their stiffness compared to the expected magnitude of adhesive/attractive forces. The normal spring constants of the cantilevers were determined using a method developed by Sader which is based on their thermal fluctuations and viscous damping [26]. The normal Q value and normal resonant frequency were determined by the thermal noise method, and the cantilever dimension was measured by optical microscopy (Nikon Optiphot 100, Tokyo, Japan) and digitally analyzed using the open software ImageJ (NIST, Gaithersburg, MD). The torsional spring constants (k_ϕ), needed for friction measurement data processing, were calculated using the method developed by Álvarez-Asencio et al. [27]. AFM experiments using contact mode were performed to obtain three different kinds of data: normal force, friction and topographic data.

2.3 Normal Force Measurements

In normal force measurements, the sample is moved toward and away from the cantilever tip by the piezoelectric scanner, and raw data are collected as cantilever deflection versus piezo movement. These raw data are converted into force versus distance through several steps as described elsewhere [23].

Normal force measurements were conducted with an approach and retraction velocities of both 4 and 1 μm/s, and triggered at 207.7 and 158.7 nN of deflection; 25–30 curves were collected in different locations on the surface.

2.4 Topography and Conventional Friction Imaging

This measurement is performed by moving the sample laterally with respect to the tip (scanning direction of 90°) and recording the tilt of the cantilever while applying a specific applied load. While the variation of the vertical cantilever deflection provides topography, the variation of the lateral deflection gives simultaneous friction information on the system. As the sample is scanned by the tip in both directions (often called trace and retrace), the AFM tip tilts in different directions, providing 2 lateral photodetector signal outputs with reversal signs for every scan line (Fig. 1). The inversion of the voltage sign is due to the torque applied to the end of tip when the scanning direction is reversed. Under perfect scanning conditions and in the absence of anisotropy, the retrace will be a mirror image of the trace.

The applied loads (that are treated in the instrument as *cantilever deflections* and controlled by the *setpoint*) were converted to force using the deflection sensitivity and the normal spring constant as for the force curves. Experiments at different applied loads over a range of the order of 10 to 150 nN were performed with a scan rate of 1.5 Hz, at load intervals of around 20 nN. A set of three images was obtained at each load, where every set contains one image with lateral photodetector signal information during trace, another during retrace and a third image with topographic information. The scan sizes were either 10 × 10 or 12 × 12 μm^2, and each image set had a resolution of 128 × 128 pixels. Since

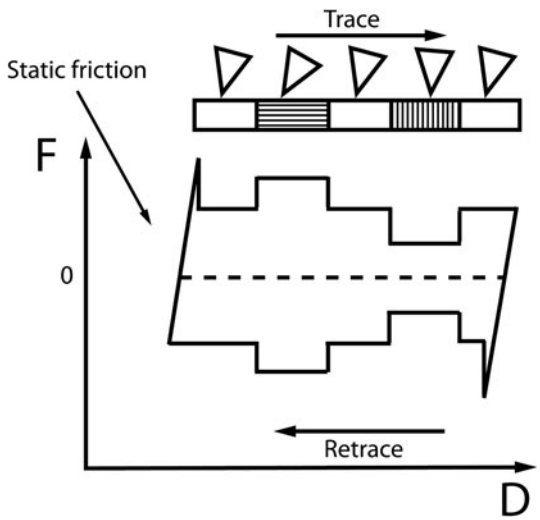

Fig. 1 Schematic representation of friction forces on the tip during trace and retrace

the images consist of pixels, they can be considered as matrixes with 128 rows and 128 columns for the calculations performed subsequent to the AFM measurements.

Afterward, lateral photodetector signal outputs, V_D (where the D refers to the trace or retrace scan *direction*), were converted to friction forces (F_D) by Eq. 3 where δ is the lateral deflection sensitivity [28], k_ϕ is the torsional spring constant (determined as described above), and h_{eff} is the effective height (the height of the tip plus half the thickness of the cantilever).

$$F_D = \frac{V_D}{h_{\text{eff}}}\frac{k_\phi}{\delta} \tag{3}$$

While this successfully converts deflection to units of Newton, zero force is determined by the baseline value, which is arbitrary. Under the assumption that the friction force is independent of the direction of motion, the issue of baseline drift can be obviated by taking the difference between the trace and retrace.

When the images were obtained, a flattening algorithm was applied in order to remove tilts from the images and correct for scan line misalignments. In practice, each scan line on the image was fitted using a linear regression and this regression was subtracted from the real data. Finally, the data average of each line, before the flattening, was added to the filtered data in order to keep them in the same range as that before applying the flattening. To obtain a friction coefficient and adhesion images, a set of lateral force images were obtained as a function of load. They were tiled and pixelwise fitted to a modified Amontons' Law (Eq. 2) to create two images where the z-axes return the friction coefficient and adhesion values, respectively, which provide a general description of the tribological response of the surface. This technique development is integrated into the following section.

3 TPM: Results and Discussions

Figure 2 shows trace, retrace and average friction force images obtained at 3 different applied loads. (7 such images are used to obtain TPM images). The set of average friction forces was created by combining trace and retrace data using Eq. 3. Such averaged friction images taken at different loads are the data subsequently used to create the friction coefficient and adhesion maps, respectively.

A linesection (black line) of 1.7 μm over the same feature is shown as an inset in every image of Fig. 2. These insets clearly demonstrate how the measured friction varies over different regions, displaying the friction during trace and retrace, and finally how the absolute difference in friction force increases with increasing applied load. The friction images displayed in Fig. 2 show clear contrast, indicating that there are different regions with significantly different frictional properties and hence presumably different composition and phases. The "particle/matrix" structure implicit from these images is consistent with earlier studies [25, 29], which show that Vancron®40 has a heterogeneous microstructure characterized by a homogeneous distribution of fine hard phase particles of carbides and carbide-nitrides in the alloy matrix.

Each of these images was obtained at a single and specific applied load; consequently, they would not provide information about friction properties at other loads and neither could they predict whether the friction contrast would vary as a function of load. For example, if the adhesion properties and friction coefficients of the different regions are very different, the contrast between different regions could change with load. A highly adhesive region might display relatively high absolute friction at a low load while nonetheless having a relatively low friction coefficient. A less adhesive region in the same image, but with a higher friction coefficient could appear to have lower friction at low loads and higher friction at high loads. Thus, it is more useful to generate images that provide tribological information independently of the specific applied load. With such images, it would be possible to fully describe friction properties of the studied system and predict friction values and contrast at any applied load.

In order to show how these images can be obtained, the calculation is simplified to two positions on the image, one located where the friction contrast is lower (x), which corresponds to the matrix in the material, and the other located in a particle where the friction is higher (+) (Fig. 2). The average friction force is extracted at each of these two pixels in each of seven images performed at different loads, and these two set of friction data were plotted with respect to the applied load in Fig. 3.

A linear regression was used to fit the data in Fig. 3 in order to extract μ (from the slope) and adhesion values (from the intersection of the line with the load axis) according to Eq. 2. These two parameters provide load-independent tribological information related to the composition and microstructure of the two pixels analyzed on the surface. Such a treatment is automatically applied pixel by pixel across the tiled images to generate friction coefficient and adhesion maps. The friction coefficients generated on the particle and the matrix are 0.75 and 0.50, respectively, and the adhesion values observed on the matrix and on the particle are relatively similar, −38.5 and −48.7 nN, respectively. These values of adhesion detected by TPM are comparable to the jump-out on the retraction arm of the normal force curves where the adhesion was obtained by multiplying the jump-out distance between the tip and the surface with the k_z of the cantilever [30]. (Note that it is essentially untenable to perform imaging at

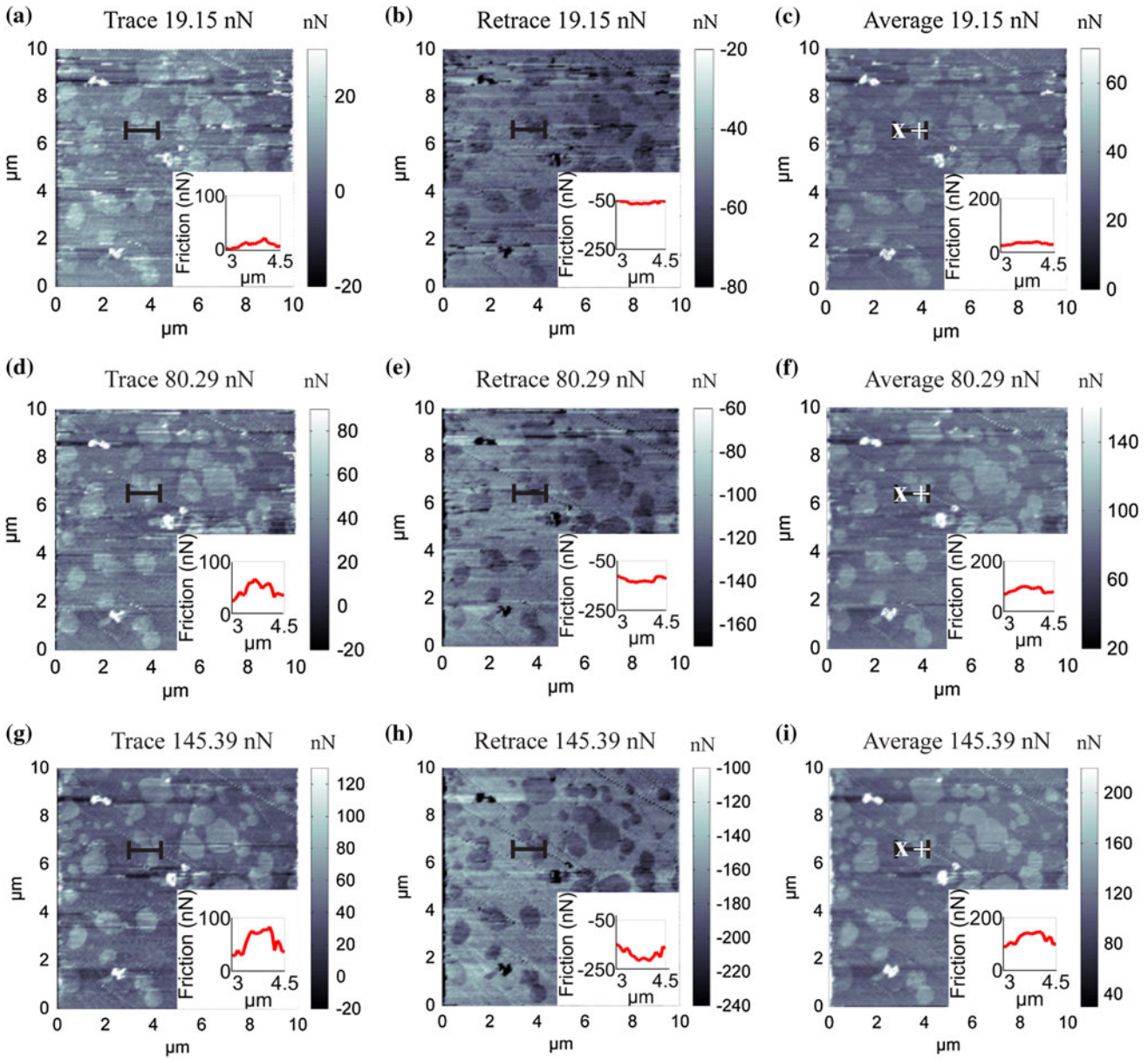

Fig. 2 Friction images of Vancron®40 obtained in air and constructed from trace (**a**, **d**, **g**), retrace (**b**, **e**, **h**) and average (**c**, **f**, **i**) LFM data for applied loads of 15.19, 80.29 and 145.39 nN. The *insets* show the variation of the friction value through a cross section of 3.7 μm

negative loads, so any small nonlinearity due to contact mechanics is inaccessible—for soft surfaces, however, this effect will be manifested even at positive loads [4] and could even be utilized for materials mapping).

We note that in this way, it is possible to extract an adhesion value from the data without actually separating the surfaces from contact and for convenience we henceforth refer to this value as "contact adhesion." This method of adhesion determination avoids several potential problems which can affect "conventional" pull-off adhesion measurements [30]. These are, for example, (1) surface sliding during the separation process, due to the finite angle between the probe and surface, with resulting relative axial motion during separation, the magnitude of which depends on the probe size [31]; (2) thermal fluctuations or mechanical noise, which otherwise may lead to underestimation of the adhesion due to the premature departure of the probe from the surface; (3) inaccessibility of the adhesion value due to either too low spring constant or large adhesion value. (In some cases, the piezo travel is insufficient to perform the adhesion measurement. In others, the adhesion value is prejudiced by departure from the linear response region of the photodiode.) Hence, as long as the modified Amontons' Law is a reasonable description

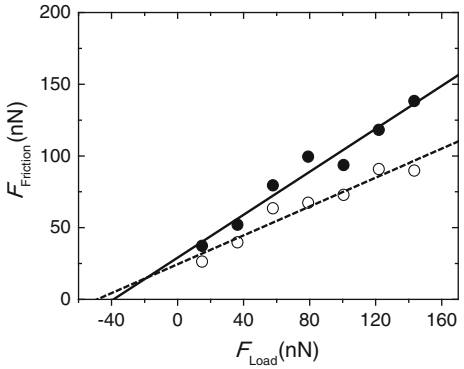

Fig. 3 Effect of applied load on friction force, at individual pixels, where the *filled* and *empty symbols* correspond to the particle (+) and matrix (x), respectively

of the friction–load relationship (which as Fig. 3 shows the case for this system), the adhesion calculated using lateral forces may be more reliable than using pull-off curves.

If the calculation of the friction coefficients and adhesion values is instead performed for every pixel in the images in Fig. 2, it is possible to obtain two images: a spatial map of the friction coefficient and a spatial map of the adhesion value (Fig. 4).

Figure 4a is a topography image taken in contact mode, which once again shows the microstructure of the alloy, that is, a matrix containing particulate features with diameters below 2 μm, which are present both above and below the matrix surface. In Fig. 4b, the friction coefficient at each pixel is mapped for the same portion of the surface as in Fig. 4a, and the image contrast is provided by the difference in friction *coefficient* rather than friction *force*. Arguably, the resolution of the different domains is even sharper than for Fig. 4a. It can be seen that the particle features systematically display a larger friction coefficient than the matrix, independently of whether they protrude or not. This implies that they may be the same or similar kind of particles. The friction coefficient values observed on the asperities ranged between 0.65 and 0.85. On the other hand, the matrix displayed a lower friction coefficient with values between 0.40 and 0.70.

Figure 4c is the equivalent contact adhesion image obtained pixelwise as in Fig. 3, and it arises solely from the lateral force data in the tiled images. While it is possible to distinguish some of the domains and correlate their position with Fig. 4a, b, contrast in the image is, however, not very good. This is probably due to the fact that the contact adhesion values are rather similar for the two materials for the case of interaction with the AFM tip in air (the adhesion is relatively constant at around −40 nN over the whole scan area). For the case of imaging in air, this is not unexpected. Since the surfaces were exposed to ambient relative humidity (19 % on this occasion), layers of water are expected to exist on the surface. Furthermore, during measurement, when the tip is close to, or in contact with the surface, a capillary bridge between the tip and the sample should also spontaneously condense, leading to an additional adhesive contribution [9], the strength of which depends on the local surface properties and the relative humidity. This bridge forms and swells during the friction measurement (capillary harvesting) [9], but is not likely to change dimensions significantly with position during scanning, and thus, its contribution to the adhesion force is likely to be highly similar, independent of position.

If the capillary effect dominates the adhesion, it becomes difficult to distinguish between matrix and hard phase particles. The capillary adhesion contributes to the friction inasmuch as it provides an extra "internal" load and therefore increases friction according to Eq. 2. The linearity of the behavior with load clearly indicates that there is no *change* in μ associated with changes in the condensate with varying load. It is worth noting that if the relative humidity becomes quite large (over the critical threshold regime of complete contact flooding) [9], the presence of water on the surfaces can change the sliding regime from "interfacial" to "lubricated" and thus appreciably alter the friction coefficient

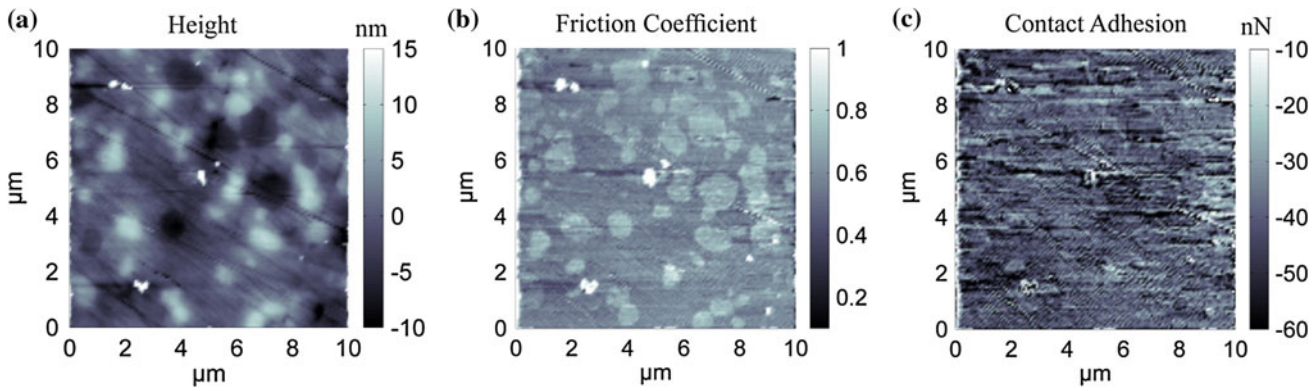

Fig. 4 Silicon-Vancron®40 images studied in air, **a** height, **b** friction coefficient and **c** contact adhesion

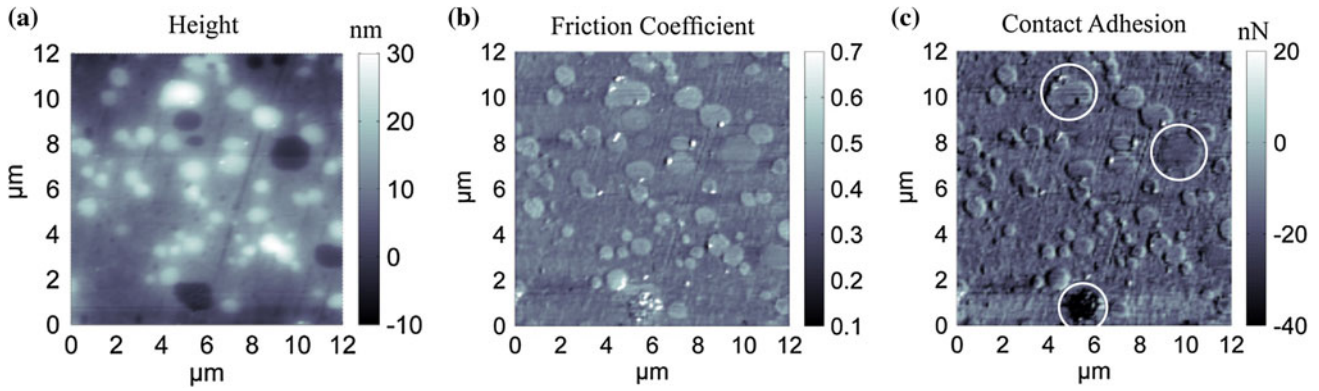

Fig. 5 Silicon-Vancron®40 images studied in tetradecane, **a** height, **b** friction coefficient and **c** adhesion. The *white circles* show features where there is clear contrast

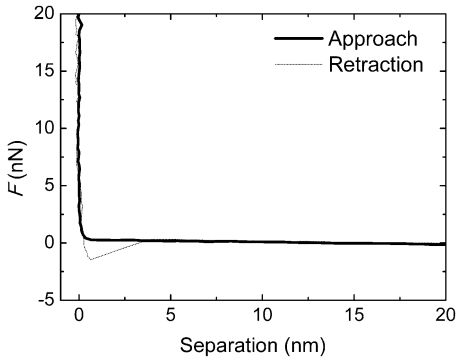

Fig. 6 Normal force curves on approach (*bold line*) and retraction between a silicon tip and Vancron®40 in tetradecane

[9, 11]. Consequently, it is very important to measure the humidity under which the experiments are performed in order to sensibly compare friction coefficients.

In liquid, however, capillary condensation does not occur (except, for example, for polar substrates in nonpolar liquids with significant water contamination [32], or for air bridges between nonpolar surfaces in a polar liquid) [33, 34]. Thus, this "equalizing" component to the adhesion is not likely to operate and the value is more likely to reflect the respective surface energies of the tip and surface regions if the experiment is performed in liquid.

This hypothesis was evaluated by performing the TPM between Vancron®40 and silicon cantilever in tetradecane, and the results are summarized in Fig. 5. This figure shows a topography image taken in contact mode, and as expected, the surface topography is similar to the case in air, that is, it consists of particulate features with diameters below 2 μm, which are present both above and below the matrix surface. This image indicates that the surface structure of the alloy is not perturbed by the liquid. Figure 5b shows a friction coefficient image, once again based on the tiling of a set of lateral force images as done in Fig. 4b where it can be observed, just as in Fig. 4b, that the particle features display a larger friction coefficient than the matrix. The friction coefficients in tetradecane are somewhat lower than those in air. This decrease in friction coefficient is due to the lubricating effect provided by the tetradecane, where the particles display friction coefficients ranging between 0.25 and 0.55 and the matrix displays values ranging between 0.25 and 0.45. The friction coefficient map also displays less noise than its counterpart in air (Fig. 4b) probably due to the absence of artifacts associated with movement of the condensate while scanning.

As expected, the contact adhesion image in Fig. 5c displays heterogeneity much more clearly than observed in air. The domains are now clearly seen in the image, and the resolution is comparable with that in Figs 4b and 5b since there is a clear difference in the adhesion values of the matrix and the particles in the absence of condensate. The adhesion contrast is partly enhanced due to edge effects around the domains (dark on the left and bright on the right)—this reflects that the tip position is slightly offset between "forward" and "back" scans, due to the friction forces it is sensing and possibly also height tracking. Such effects are intrinsic features of scanning probe imaging, though usually appear asymmetric due to the selection of only one imaging direction. Nonetheless, the image clearly shows different colors for different domains, indicating distinctly different properties.

With the immersion of the system in liquid, the capillary forces were eliminated and adhesion force values related to the surface properties of the alloy microstructure are observed in Fig. 5c. The particles display adhesion values ranging between −10 and −40 nN and the matrix values ranging between approximately −15 and −25. These contact adhesion values are larger than the example of adhesion value of −3 nN obtained from the jump-out of the retraction force curve (e.g., in Fig. 6) by pull-off measurements.

In this case, where no capillary condensate contributes to the adhesive interaction, the artifacts discussed earlier are expected to have large effect on the pull-off force. We surmise that this is the reason for the much lower adhesion values obtained from the force curves.

Finally, it is worth noting that while Eq. 2 represents a simplified form of the true friction–load relationship, it appears to be justified by the data. For a softer substrate, there would be no hinder to fitting the tiled pixel data to a more complex, nonlinear friction versus load relationship, which would reflect the deformation of the material and could be used to instead return the shear stress and elastic modulus in addition to the friction coefficient and adhesion.

4 Conclusions

For the first time, tribological properties mapping (TPM) has been performed based on lateral atomic force microscope data. TPM includes three-dimensional, quantitative maps of friction coefficients and contact adhesion force.

Application of the TPM mapping to Vancron®40 shows that the matrix/particle microstructure of this tool alloy is equally well revealed by friction coefficient or contact adhesion as by topography. It can thus be used as a complementary technique which not only provides clues to the material composition of the different phases, but can also be used to predict the nanotribological properties of the surface, based on the distribution, relative abundance and height of the different components.

The contact adhesion values extracted from the friction curves were systematically larger than the values extracted from the retraction curves of force measurements. The fact that there is no need to separate the tip from the surface to obtain the adhesion means that the approach avoids several artifacts associated with conventional adhesion measurements. It may well be that the contact adhesion value is a more useful and representative quantity than the conventional pull-off force.

Capillary condensates cause an additional adhesive contribution, and the relative invariance of the dimensions of the condensate as it scans over the surface means that this contribution leads to poor spatial resolution of adhesion in air. This is likely to be equally a problem for techniques such as so-called chemical force microscopy, where force curves are performed at each point on the surface. Even worse, the inability of such a condensate to equilibrate might lead to further rate-dependent artifacts for such techniques. In the absence of such condensates, for example, upon immersion in liquid, the contact adhesion map displayed high resolution and was very sensitive to the surface composition.

As for any other imaging technique, the most important resolution-limiting factor in TPM is the size of the probe. When the tip radius is larger than the topographic features, artifacts such as edge effects and probe imaging are unavoidable. For a smooth surface, however, with varying only in tribological properties, then the resolution is essentially controlled by the pixel size.

In this scanning technique, TPM provides powerful complementary information to conventional imaging and in particular allows the tribological behavior to be better related to microstructure.

Acknowledgments This project is part of the program "Microstructure, Corrosion and Friction Control" financed by SSF, the Swedish foundation for Strategic Research. We also thank the Swedish Research Council for financial support. Uddeholms AB, Sweden, is acknowledged for supplying the Vancron®40 samples and the microstructure information of the alloy. Useful discussions with Gunnar Dunér and Emily Cranston are gratefully acknowledged.

References

1. Svagan, A.J., Azizi Samir, M.A.S., Berglund, L.A.: Biomimetic polysaccharide nanocomposites of high cellulose content and high toughness. Biomacromolecules **8**(8), 2556–2563 (2007)
2. Thormann, E., Mizuno, H., Jansson, K., Hedin, N., Fernandez, M.S., Arias, J.L., Rutland, M.W., Pai, R.K., Bergstrom, L.: Embedded proteins and sacrificial bonds provide the strong adhesive properties of gastroliths. Nanoscale **4**(13), 3910–3916 (2012)
3. Sababi, M., Ejnermark, S., Andersson, J.r., Claesson, P.M., Pan, J.: Microstructure influence on corrosion behavior of a Fe-Cr-VN tool alloy studied by SEM/EDS, scanning Kelvin force microscopy and electrochemical measurement. Corros. Sci. **66**, 153–159 (2013)
4. Bogdanovic, G., Tiberg, F., Rutland, M.W.: Sliding friction between cellulose and silica surfaces. Langmuir **17**(19), 5911–5916 (2001)
5. Israelachvili, J.: Surface forces and microrheology of molecularly thin liquid films. In: Nhushan, B. (ed.) Handbook of micro/nano tribology. CRC Press, Boca Raton (1995)
6. Derjaguin, B.: Molekulartheorie der äußeren reibung. Zeitschrift für physik a hadrons and nuclei **88**(9), 661–675 (1934)
7. Berman, A., Drummond, C., Israelachvili, J.: Amontons' law at the molecular level. Tribol. Lett. **4**(2), 95–101 (1998)
8. Gao, J., Luedtke, W.D., Gourdon, D., Ruths, M., Israelachvili, J.N., Landman, U.: Frictional forces and Amontons' law: From the molecular to the macroscopic scale. J. Phys. Chem. B **108**(11), 3410–3425 (2004)
9. Feiler, A.A., Jenkins, P., Rutland, M.W.: Effect of relative humidity on adhesion and frictional properties of micro- and nano-scopic contacts. J. Adhes. Sci. Technol. **19**(3–5), 165–179 (2005)
10. Plunkett, M.A., Feiler, A., Rutland, M.W.: Atomic force microscopy measurements of adsorbed polyelectrolyte layers. 2. Effect of composition and substrate on structure, forces, and friction. Langmuir **19**(10), 4180–4187 (2003)
11. Feiler, A.A., Stiernstedt, J., Theander, K., Jenkins, P., Rutland, M.W.: Effect of capillary condensation on friction force and adhesion. Langmuir **23**(2), 517–522 (2006)
12. Pilkington, G.A., Thormann, E., Claesson, P.M., Fuge, G.M., Fox, O.J.L., Ashfold, M.N.R., Leese, H., Mattia, D., Briscoe,

W.H.: Amontonian frictional behaviour of nanostructured surfaces. Phys. Chem. Chem. Phys. **13**(20), 9318–9326 (2011)
13. Thormann, E., Yun, S.H., Claesson, P.M., Linnros, J.: Amontonian friction induced by flexible surface features on microstructured silicon. ACS Appl. Mater. Interfaces **3**(9), 3432–3439 (2011)
14. Yamada, S., Israelachvili, J.: Friction and adhesion hysteresis of fluorocarbon surfactant monolayer-coated surfaces measured with the surface forces apparatus. J. Phys. Chem. B **102**(1), 234–244 (1998)
15. Bowden, F.P., Tabor, D.: Mechanism of metallic friction. Nature **150**, 197–199 (1942)
16. Butt, H.-J.r., Graf, K., Kappl, M.: Physics and chemistry of interfaces, 2nd, rev. and enl. ed. Wiley-VCH, Weinheim (2006)
17. Sasaki, K., Koike, Y., Azehara, H., Hokari, H., Fujihira, M.: Lateral force microscope and phase imaging of patterned thiol self-assembled monolayer using chemically modified tips. Appl. Phys. A **66**, 1275–1277 (1998)
18. Baselt, D.R., Baldeschwieler, J.D.: Lateral forces during atomic force microscopy of graphite in air. J. Vac. Sci. Technol. B **10**(5), 2316–2322 (1992)
19. McMullen, R.L., Kelty, S.P.: Investigation of human hair fibers using lateral force microscopy. Scanning **23**(5), 337–345 (2001)
20. Smith, J.R., Swift, J.A.: Lamellar subcomponents of the cuticular cell membrane complex of mammalian keratin fibres show friction and hardness contrast by AFM. J. Microsc. **206**(3), 182–193 (2002)
21. Sidouni, F.Z., Nurdin, N., Chabrecek, P., Lohmann, D., Vogt, J., Xanthopoulos, N., Mathieu, H.J., Francois, P., Vaudaux, P., Descouts, P.: Surface properties of a specifically modified high-grade medical polyurethane. Surf. Sci. **491**(3), 355–369 (2001)
22. Levi, M.D., Cohen, Y., Cohen, Y., Aurbach, D., Lapkowski, M., Vieil, E., Serose, J.: Atomic force microscopy study of the morphology of polythiophene films grafted onto the surface of a Pt microelectrode array. Synth. Met. **109**(1–3), 55–65 (2000)
23. Ralston, J., Larson, I., Rutland, M.W., Feiler, A.A., Kleijn, M.: Atomic force microscopy and direct surface force measurements—(IUPAC technical report). Pure Appl. Chem. **77**(12), 2149–2170 (2005)
24. Breakspear, S., Smith, J.R., Nevell, T.G., Tsibouklis, J.: Friction coefficient mapping using the atomic force microscope. Surf. Interface Anal. **36**(9), 1330–1334 (2004)
25. Hatami, S., Nafari, A., Nyborg, L., Jelvestam, U.: Galling related surface properties of powder metallurgical tool steels alloyed with and without nitrogen. Wear **269**(3–4), 229–240 (2010)
26. Sader, J.E., Chon, J.W.M., Mulvaney, P.: Calibration of rectangular atomic force microscope cantilevers. Rev. Sci. Instrum. **70**(10), 3967–3969 (1999)
27. Álvarez-Asencio, R., Pan, J., Thormann, E., Rutland, M.W.: Determination of torsional spring constant of AFM cantilevers: Combining normal spring constant and classical beam theory. (2012). Rev. Sci. Instrum. (2013) (Submitted)
28. Bogdanovic, G., Meurk, A., Rutland, M.W.: Tip friction-torsional spring constant determination. Colloid Surf. B **19**, 397–405 (2000)
29. Heikkilä, I., Van der Heíde, E., Stam, E.D., Giraud, H., Lovato, G., Akdut, N., Clarysse, F., Caenen, P.: Tool material aspects in forming of stainless steel with easy-to-clean lubricants. Innovations in metal forming. Brescia, Italy (2004)
30. Cappella, B., Dietler, G.: Force-distance curves by atomic force microscopy. Surf. Sci. Rep. **34**(1–3), 1–104 (1999)
31. Johanna, S., Mark, W.R., Phil, A.: A novel technique for the in situ calibration and measurement of friction with the atomic force microscope. Rev. Sci. Instrum. **76**(8), 083710 (2005)
32. Feiler, A.A., Bergstrom, L., Rutland, M.W.: Superlubricity using repulsive van der Waals forces. Langmuir **24**(6), 2274–2276 (2008)
33. Thormann, E., Simonsen, A.C., Hansen, P.L., Mouritsen, O.G.: Force trace hysteresis and temperature dependence of bridging nanobubble induced forces between hydrophobic surfaces. ACS Nano **2**(9), 1817–1824 (2008)
34. Carambassis, A., Jonker, L.C., Attard, P., Rutland, M.W.: Forces measured between hydrophobic surfaces due to a submicroscopic bridging bubble. Phys. Rev. Lett. **80**(24), 5357–5360 (1998)